Materials Today Advances 2 (2019) 100011

Contents lists available at ScienceDirect

Materials Today Advances

journal homepage: www.journals.elsevier.com/materials-today-advances/

Four-dimensional imaging and quantification of viscous flow sintering within a 3D printed bioactive glass scaffold using synchrotron X-ray tomography

A. Nommeots-Nomm [a, *], C. Ligorio [b], A.J. Bodey [c], B. Cai [d], J.R. Jones [e], P.D. Lee [f, g], G. Poologasundarampillai [h, **]

[a] Department of Materials and Mining, McGill University, Montreal, Canada
[b] School of Materials, University of Manchester, Manchester, M13 9PL, UK
[c] Diamond Light Source, Oxfordshire, OX11 0DE, UK
[d] School of Metallurgy and Materials, University of Birmingham, Birmingham B5 7EG, UK
[e] Department of Materials, Imperial College London, London, SW7 2AZ, UK
[f] Mechanical Engineering, University College London, Torrington Place, London, WC1E 7JE, UK
[g] Research Complex at Harwell, Didcot, OX11 0FA, UK
[h] School of Dentistry, Institute of Clinical Sciences, University of Birmingham, Birmingham, B5 7EG, UK

ARTICLE INFO

Article history:
Received 27 February 2019
Received in revised form
2 April 2019
Accepted 1 May 2019
Available online xxx

Keywords:
Glass
Sintering
In situ x-ray tomography
Bioactive
Scaffold
Viscous flow

ABSTRACT

Bioglass® was the first material to form a stable chemical bond with human tissue. Since its discovery, a key goal was to produce three-dimensional (3D) porous scaffolds which can host and guide tissue repair, in particular, regeneration of long bone defects resulting from trauma or disease. Producing 3D scaffolds from bioactive glasses is challenging because of crystallization events that occur while the glass particles densify at high temperatures. Bioactive glasses such as the 13–93 composition can be sintered by viscous flow sintering at temperatures above the glass transition onset (T_g) and below the crystallization temperature (T_c). There is, however, very little literature on viscous flow sintering of bioactive glasses, and none of which focuses on the viscous flow sintering of glass scaffolds in four dimensions (4D) (3D + time). Here, high-resolution synchrotron-sourced X-ray computed tomography (sCT) was used to capture and quantify viscous flow sintering of an additively manufactured bioactive glass scaffold in 4D. In situ sCT allowed the simultaneous quantification of individual particle (local) structural changes and the scaffold's (global) dimensional changes during the sintering cycle. Densification, calculated as change in surface area, occurred in three distinct stages, confirming classical sintering theory. Importantly, our observations show for the first time that the local and global contributions to densification are significantly different at each of these stages: local sintering dominates stages 1 and 2, while global sintering is more prevalent in stage 3. During stage 1, small particles coalesced to larger particles because of their higher driving force for viscous flow at lower temperatures, while large angular particles became less faceted (angular regions had a local small radius of curvature). A transition in the rate of sintering was then observed in which significant viscous flow occurred, resulting in large reduction of surface area, total strut volume, and interparticle porosity because the majority of the printed particles coalesced to become continuous struts (stage 2). Transition from stage 2 to stage 3 was distinctly obvious when interparticle pores became isolated and closed, while the sintering rate significantly reduced. During stage 3, at the local scale, isolated pores either became more spherical or reduced in size and disappeared depending on their initial morphology. During stage 3, sintering of the scaffolds continued at the strut level, with interstrut porosity reducing, while globally the strut diameter increased in size, suggesting overall shrinkage of the scaffold with the flow of material via the strut contacts.

This study provides novel insights into viscous flow in a complex non-idealized construct, where, locally, particles are not spherical and are of a range of sizes, leading to a random distribution of interparticle porosity, while globally, predesigned porosity between the struts exists to allow the construct to support tissue growth. This is the first time that the three stages of densification have been

* Corresponding author.
** Corresponding author.
E-mail addresses: amy.nomm@mcgill.ca (A. Nommeots-Nomm), G.Poologasundarampillai@bham.ac.uk (G. Poologasundarampillai).

https://doi.org/10.1016/j.mtadv.2019.100011

captured at the local and global scales simultaneously. The insights provided here should accelerate the development of 3D bioactive glass scaffolds.

1. Introduction

Bioglass® was the first synthetic material to form a chemical bond with human bone and soft tissue [1]. The composition of Bioglass 45S5 allows for local ionic dissolution of calcium, phosphorous, and silicon species, which stimulates bone formation through the upregulation of seven families of genes in osteoblastic cells [2]. This enabled NovaBone LLC (Jacksonville, FL) to obtain approval for the claim of 'osteostimulation' as a property of Bioglass from the Food and Drug Administration [3]. However, the development of three-dimensional (3D) porous scaffolds for the regeneration of new bone tissue in load-bearing defects has been limited [3].

The original 45S5 bioactive glass is produced via a melt quench processing method, where a molten viscous glass is rapidly quenched, most commonly by being poured into deionized water, to form a brittle glass frit; the glass is then ground to a fine powder for clinical use. To form a 3D construct for loaded bone repair from a bioactive glass, the glass powder is mixed with an organic binder, which is then shaped into a 3D architecture via casting, foaming, or 3D printing; this is referred to as a green body [4–6]. The green body is then sintered by heating it to above the glass transition temperature (T_g) to remove the binder and fuse the glass particles together via viscous flow sintering [7].

The limitation of the original 45S5 composition is its sinterability [4]. 45S5 has a limited temperature window between its T_g and the start of crystallization (T_c) [8–10]. If crystallization occurs [11], it results in retardation of its dissolution characteristics [10] and, as a consequence, its bioactivity. Therefore, a compromise has to be met between producing mechanically robust scaffolds which are fully sintered and bioactivity; it is this issue that has limited the success of formulating 3D constructs from 45S5 for bone regeneration.

To be able to produce mechanically robust scaffolds, researchers focused on developing alternative glass compositions [12] by incorporating other cations, including those that also add additional therapeutic benefits [13], or using alternative glass-forming systems such as borate [14–17] or phosphate [18,19]. The 13-93 composition utilizes magnesium and potassium to extend its sintering window (54.6 SiO_2, 22.1 CaO, 6.0 Na_2O, 1.7 P_2O_5, 7.9 K_2O, and 7.7 MgO, in mol%) to offer enhanced sinterability while maintaining bioactivity [20]. Fugerland et al. [21] investigated the thermal properties of 13–93 monoliths and particles of the size 300–500 μm and showed there was no overlap between the nucleation and growth domains in their thermographs, making it possible to heat the glass to 800 °C before crystallization occurred. This enhanced thermal stability enables the use of fine particles during processing, which are relatively resistant to crystallization during sintering compared with other bioactive glasses [5,22–24]. Therefore, 3D scaffolds can be produced from the 13–93 composition via a variety of processing methods with various designed porosities and mechanical properties [5,16,17,22,24,25].

When producing 3D scaffolds with designed porosity, the aim is to sinter the individual glass particles into a continuous material while maintaining the overall 'designed' porous architecture. As the material sinters, if there is no net loss of material, its overall density increases, resulting in total volume shrinkage. This shrinkage should be predesigned into the scaffold architecture. The robocasting, or robocasting 3D printing process, allows for high volume fractions (>40%) of glass to be 3D printed in a layer-by-layer process which results in good sintering. Furthermore, the aligned strut geometries with linear pore connections allow for the material to be continuous in the z direction, which can withstand large compressive loads, making direct ink writing a 'go-to' technique for scaffold production [6].

Sintering of glasses at temperatures above their glass transition temperature has been studied through theoretical and computational models [26–28], but only few experiments exist to validate these models. It is known that glass densification above the glass transition temperature is controlled via viscous flow due to the effects of surface tension and capillary forces [7,29]. The theories that exist to explain this phenomenon are commonly based on 'perfect spheres,' whereas melt-derived glass powders are angular [30]. Recent work by Reis et al. [31] compared jagged angular particles with spherical particles during sintering of a MgO–CaO–SiO_2 glass. Their work supported previous studies showing that sintering rates of jagged particles are significantly faster than those of a spherical counterpart [32,33]. Reis et al. [31] went further to present a model to measure the anisotropy experienced during sintering of the more angular particles, highlighting the importance of differentiating particle shape when studying viscous flow sintering.

To date, the most commonly used method to understand the sintering of glasses is to study changes in viscosity with temperature, by characterizing the glasses' transitions via isothermal or dynamic differential scanning calorimetry (DSC) [34–39] or hot stage microscopy [40,41]. However, neither of these techniques provides insights into the morphological changes taking place at scales of the glass particles (local scale). Characterizing the sintering mechanisms of bioactive glasses has added complications because of their tendency to crystallize and the subtle changes in the thermal properties when measured by DSC. Crystallization during sintering can alter the viscosity of the glasses and the local chemistry, consequently affecting their ability to flow and coalesce at high temperatures [42]. Once glasses crystallize, the sintering mechanism changes from classical viscous flow to a grain growth–based mechanism.

Recently, micro–computed tomography (μCT) has been used to study the glass sintering behavior. Published work has focused on soda-lime-silica glasses because of their resistance to crystallization, well-characterized thermal properties, and readily available spherical powders at various particle sizes [43–47]. Villanova et al. [47] performed 4D X-ray tomography on in situ sintering of soda-lime-silica glass particles. Their work discusses the limitations of the current theories surrounding sintering practice, suggesting that the classical Frenkel two-sphere sintering theory does not translate to the third dimension [47]. This conclusion is not surprising because it is well documented that the model has many limitations [48], especially surrounding the exclusion of glass temperature–dependent viscosity and the Frenkel equation's reliance on Newtonian flow.

Here, for the first time, we use 4D synchrotron X-ray tomography to map the sintering of a 3D printed bioactive glass scaffold synthesized from the 13–93 composition. We report novel insights into the structural changes taking place (with a submicron voxel

size) and present a visualization of how viscous flow sintering of bioactive glasses takes place in 3D constructs over time.

2. Methodology

2.1. Scaffold preparation

All materials were purchased from Sigma Aldrich (Dorset, UK), unless otherwise stated.

Bioactive glass 13–93 with nominal composition (mol.%) 54.6 SiO_2, 22.1 CaO, 6.0 Na_2O, 7.7 MgO, 7.9 K_2O, and 1.7 P_2O_5 was manufactured via melt quenching of silica (Prince Minerals, Stoke-on-Trent, UK), sodium carbonate, calcium carbonate, and phosphate [5]. Inks for 3D printing were produced from 25 wt% Pluronic F-127 (CAS: 9003-11-6), using a volume ratio of 47.5 vol% glass to Pluronic solution, with a glass particle size distribution ranging from 3.3 to 30.5 μm and $D_{50} = 10.8$ μm. Inks were mixed using a Thinky ARE-100 mixer, until homogenized. Scaffolds were then printed using a 3D robocaster (RoboCAD 3.0; 3D Inks, Stillwater, OK) with a 250-μm-diameter cylindrical nozzle (Nordson LTD., UK) on to an overhead projector paper; 20 mm of ink was extruded (known as the 'lead-in') before scaffold printing to ensure flow was homogenous within the printed part. Both the lead-in and the scaffolds were printed at a speed of 4 mm/s. Printing was performed under humidity of 60–80% and at a temperature of 23 °C (full details of printing protocol can be found in the study by Nommeots-Nomm et al. [24]).

2.2. In situ X-ray tomography of sintering

In situ synchrotron X-ray microtomography was performed at the Diamond Manchester Imaging Branchline I13-2 of Diamond Light Source (DLS) [49,50]. Fig. 1 shows a schematic of the experimental setup used. Bioactive glass scaffolds (1.8 mm × 1.8 mm × 1.8 mm) were sintered in the bespoke proportional- integral-derivative-controlled 'Laura' furnace [51–54]. The scaffolds were glued on an alumina sample holder using a high-temperature glue (OMEGABOND 600; Omega LTD, UK). The alumina holder was then mounted on to a rotating spindle on the sample stage. Sintering was conducted via a two-stage process; the sample was heated to 500 °C at a heating rate of 3 °C/min for the first isotherm for 1 h (binder removal), followed by a ramp at 3 °C/min to the sintering temperature of 700 °C (glass sintering). Samples were held at this temperature for 2.5 h, and then the furnace was cooled.

X-ray microtomography was performed with a filtered (1.3 mm pyrolytic graphite and 3.2 mm Al filters) pink (polychromatic) beam with energy in the range of 8–30 keV. A 500-μm-thick $CdWO_4$ scintillator–coupled sCMOS (2560 × 2160 pixels) detector (pco.edge 5.5; PCO AG, Germany) positioned 75 mm from the sample was used to capture the transmitted X-rays (projections). Scans were performed with a total optical magnification of 8×, resulting in an effective isotropic pixel size of 0.81 μm. X-ray projections of the scaffold were recorded with an angular step size of 0.2° and an exposure time of 45 ms for each image until 655 °C (901 projections over 180°). From 655 °C, the exposure time was reduced to 35 ms, and after 20 min of reaching 700 °C, the exposure time was set to 45 ms and the step size to 0.15° (1201 projections). Dark- and flat-field images were recorded at the beginning and end of the experiment. Projections were reconstructed into tomograms using a filtered back projection algorithm incorporating dark- and flat-field correction and ring artifact suppression [55–58].

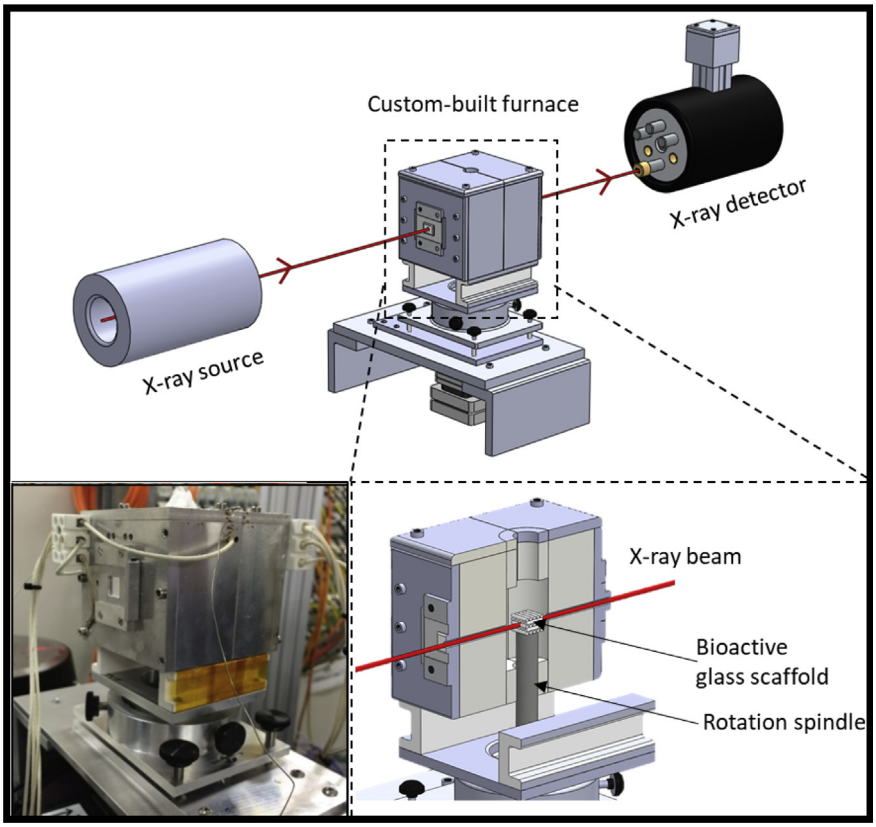

Fig. 1. Experimental setup on beamline I13 at the Diamond Light Source synchrotron facility. A photograph of the custom-built furnace used in the experiment and schematic of its internal chamber are shown in the insets.

2.3. Three-dimensional image analysis

Before the 3D image analysis, data were first processed following a similar methodology to that established in the studies by Lee and Hunt [59], Chaijaruwanich et al [60], and Jones et al. [61]. Processed images were then thresholded and analyzed for the surface area, strut diameter, strut-to-strut spacing, and intrastrut voids of the scaffolds. Full details on image processing and analysis performed can be found in the Supplementary Information S1.

3. Results and discussion

High-resolution synchrotron X-ray microtomography was used to study the 3D structural changes with sintering (4D) of a printed scaffold. Fig. 2(a) and (b) show 3D renderings of the printed 13–93 bioactive glass scaffold before (green body state) and after sintering. The magnified image (inset of Fig. 2 (a)) shows the particles within the green body were tightly packed enabling it to support the 3D printed scaffold structure during the sintering process. Fig. 2 (b and b-inset) shows the scaffold after sintering where almost complete sintering has been achieved. The once discrete particles coalesced together to form continuous struts which are bonded to each other at the intersecting junctions. Furthermore, with sintering, the surface of the scaffold struts becomes smooth. Fig. 2(b) shows that there are several pores present within the struts, suggesting that the scaffold does not achieve 100% densification, as also eluded by the fracture surface scanning electron microscopy (SEM) images presented in Supplementary Information S2.

The in situ tomographic scans (single tomogram every 35 to 55 s) performed during the sintering cycles allowed for dynamic visualization of microstructural evolution in 3D and quantification of the changes. Supplementary Information S3 and S4 show videos of the morphological evolution on a plane through the entire scaffold (S2-global) and through a single strut (S3-local), visualizing scaffold densification and particle coalescence, respectively. As the glass is heated to above ~650 °C, the particles begin to merge and coalesce to form a denser solid by the reduction of surface area via viscous flow sintering [7].

The morphological evolution could be quantified as a function of time and temperature by calculating the total surface area (Fig. 2 (c)) and relative density of the scaffold (Fig. 2 (d)). Fig. 2 (c) shows three distinct rate changes in surface area. This is very well correlated with the traditional three zones, or stages, that occur during sintering. Furthermore, the measured changes in scaffold density with time (Fig. 2 (d)) fall very well within these three distinct stages. Stage 1 is where initial necks are formed between the previously discrete particles; here, sintering is slow with a relatively small change in surface area and 5% increase in the relative density (Fig. 2 (d)). Stage 2 is the intermediate stage where the majority of sintering takes place. Here, the particles transform into a bulk material, where particles are no longer able to be resolved as individual ones and instead have coalesced into a continuous material via viscous flow. This is driven and quantified by the large drop in surface area (Fig. 2 (c)) and 35% increase in relative density (Fig. 2 (d)) of the glass. This change in densification across the scaffold is clearly visible in S3 and S4, occurring within a 16-minute window once the glass had reached 680 °C.

The tempearture dependence of glass viscosity can be modeled by the MYEGA model [62], which is deemed the most accurate method of determining the change in viscosity with temperature across the whole temperature range. Here, we used the data provided in the study by Fu et al. [63] for the 13–93 composition to plot the relationship of viscosity and temperature (Fig. S2(i)). It is reported that glasses do not sinter until their viscosities are below

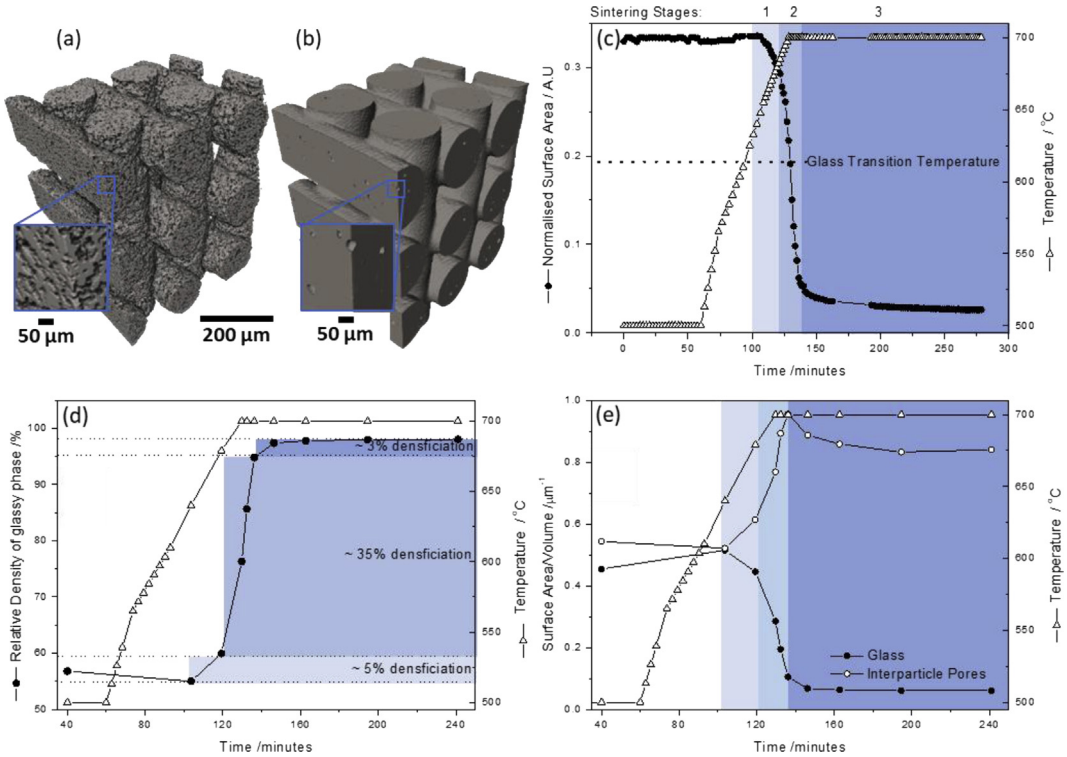

Fig. 2. (a) 3D rendering of the glass in its presintered green body state (scale bar 200 µm) and (b) post-sintered state (scale bar 200 µm); the insets highlight the changes observed (scale bar 50 µm); (c) changes in normalized surface area with time and temperature during sintering; (d) relationship between relative density with time and temperature during sintering; (e) changes in the relative ratio between surface area and volume with sintering time and temperature of the glass phase and interparticle porosity. All graphs are related to the three stages of sintering, stages 1, 2, and 3, via shaded blue regions.

10^7 Pa s [64], correlating to the data obtained with the MYEGA model [62,63] in S2 (i); it can be seen that stage 2 sintering occurs once the viscosity had reduced to this value at ~680 °C.

Stage 3 is the final stage of sintering where, if energetically favorable, the isolated pores are removed from the glass structure [65]. Here, the measured relative density increased by a further 3% and a small drop in surface area. As the glass is heated and moves through these three stages, the viscosity is constantly reducing (S2 (i)) until the isotherm is met at 700 °C. If the glass stays amorphous during sintering, the temperature-dependent viscosity of the glass will continue to facilitate flow and densification. The three defined stages are individually colored in each figure for easy identification throughout the article.

Upon completion of sintering, after 2.5 h at 700 °C, the scaffold had a 98% relative density. The remaining 2% of the strut volume was occupied by isolated pores remaining in the scaffolds (Fig. 2(b)). Fig. 2 (e) shows the change upon sintering in a small section of a scaffold strut with time and temperature of the two phases, glass and the interparticle pore, surface area (SA), normalized by their volume (SA/V). (Fig. S1 shows details on how sections were obtained.) As expected, the relative surface area of the glass, with respect to its volume, decreased throughout sintering. The total volume of glass remained constant throughout; hence, the decrease in the SA/V was driven by the reduction in the total surface area of the scaffold, i.e., densification via viscous flow. Once sintering entered stage 3, both the volume and surface area remained constant; therefore, a plateau was reached. The trends observed agree to the trends in surface area (Fig. 2 (c)) of the whole scaffold and to the changes observed in relative density in Fig. 2 (d).

Fig. 2 (e) also shows the evolution of SA/V vs. time and temperature for the interparticle pores. While the total volume of the glass particles remained constant, the total volume of the pores within the struts decreased, so did its total surface area. Therefore, the surface area, averaged by its volume, gives an insight into the

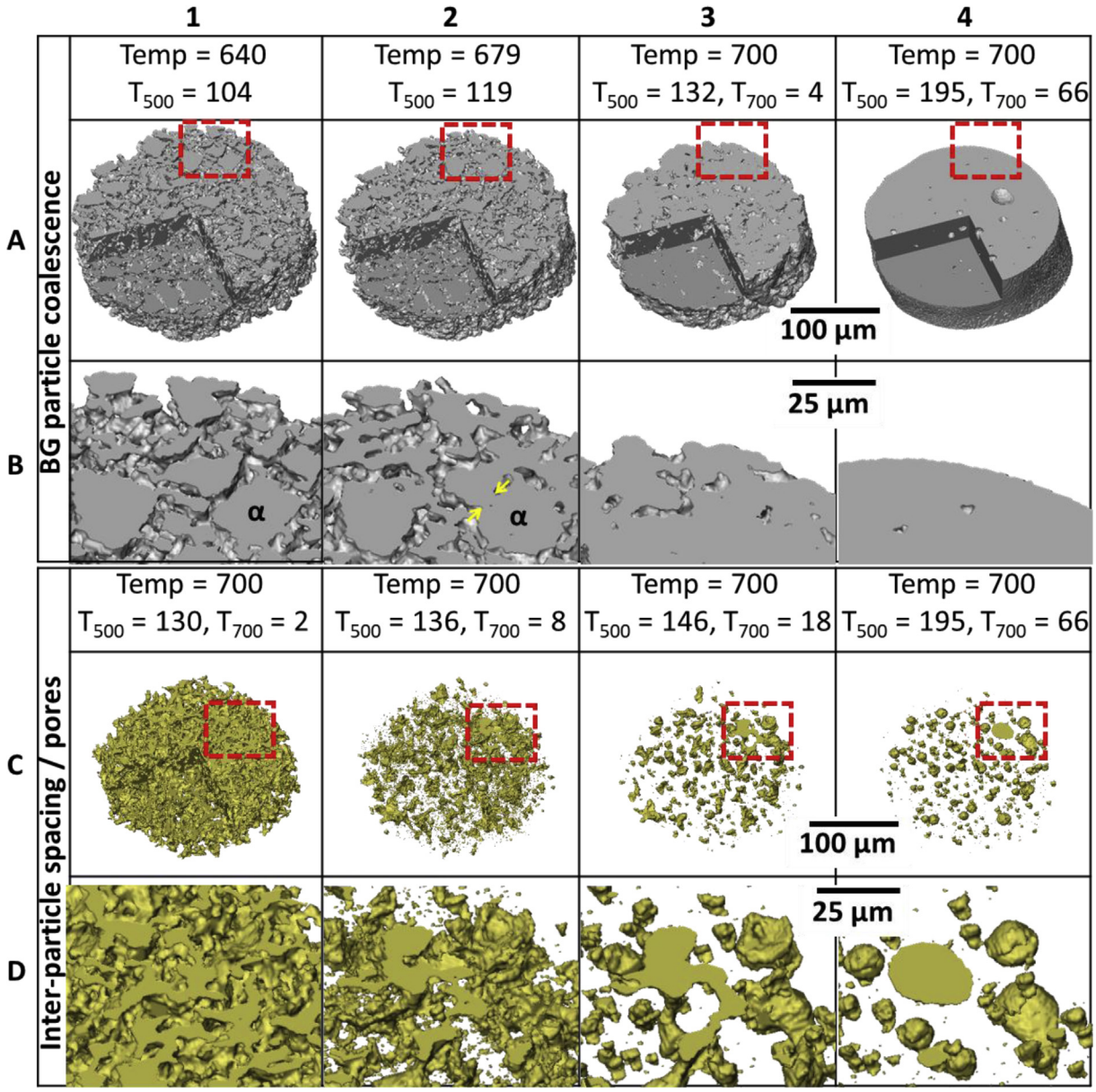

Fig. 3. A 3D reconstructed volume of a small section of a scaffold strut showing the bioactive glass (BG) (A,B) and inter-particle spacing (pores) (C,D) phases sequentially with time and temperature. The lower images (C and D) are magnified areas of the red boxes in A and D. Yellow arrows indicate neck formation between particle α and one of its neighbors.

rates of densification/removal of the pores present. Before the start of sintering (at approximately 640 °C), both glass and pores had similar SA/V (0.5 μm^{-1}) because the 3D printed scaffolds had an initial solid packing of 47.5 vol%. At this temperature, both the glass and the pores were highly interconnected. Once sintering started, pore volume decreased with decreasing surface area. Within the plot, there was an increase in SA/V, suggesting that the rate of decrease in the total volume was higher than the reduction in surface area. At the end of stage 2 (temp = 700 °C, time = 5 min), a spike in SA/V was observed, which then reduced to a plateau at 0.82 μm^{-1}. Morphological observations at these corresponding temperatures and times shed light on the mechanisms for this spike.

Rows A and B of Fig. 3 (B zoomed in region of the red square in A) show 3D sCT images of a child volume of a 13–93 bioactive glass strut at different sintering times and temperatures. A child volume is refferring to a sub-section of the original scaffold with a reduced volume. At 640 °C (A1 and B1), individual particles of different shapes and sizes were seen; in particular, several large particles such as 'α' were observed with faceted surfaces remaining from the ball milling process (supporting particle size distribution and SEM image are in S2). Between temperatures of 640 °C and 679 °C (A2 and B2), very fine particles merged with neighboring larger particles and the faceted surfaces of the large particles became rounded (α in B2) [31]. The smaller particles have the largest surface-to-volume ratio and therefore flow at lower temperatures compared with the larger particles present. Furthermore, formation of necks, indicated by yellow arrows in B2, and ligament bridges between neighboring glass particles were also observed throughout. We saw no evidence of particle rearrangement during sintering.

The particle size range resulted in a non-uniform packing of particles throughout the green body, which resulted in non-uniform sintering during stage 1, with some areas 'flowing' preferentially depending on their inital particle size [65]. Particle size distribution and preferential sintering can alter local glass viscosities and the formation of interconnected pores between different sintering rates of the particles present [66]. At the end of stage 1, the larger particles were still recognizable. Fig. 3 (A3) and (B3) highlight the change in densification obtained at 700 °C The prescribed sintering temperature is 700 °C, determined experimentally in the literature for this glass composition [22]. At this temperature, all the glass particles within the size range used in this study should have enough energy for viscous flow. Here, defined as Stage 2, we saw formation of the densified struts with no individual particles remaining. This process is primarily driven by capillary forces and reduction in surface area. Therefore, at the macroscale, the scaffold sintered homogeneously, even though at a mesoscale, this was not the case. After 66 min at 700 °C (Fig. 3 A4 and B4), the strut surface was smooth and almost fully dense with some isolated pores left within the structure. This is supported by SEM images in S2 (e) (g). Comparing Fig. 3 (A1–A4), it is evident that the overall diameter of the strut decreased with sintering. This supports experimental studies demonstrating that sintering of 13–93 scaffolds for 1 h at 700 °C is effective [5,22,24].

Rows C and D of Fig. 3 show the interparticle pore structural evolution within the same child volume of 13–93 bioactive glass strut as in Fig. 3 (A). Fig. 3 (C1) and (D1) show the pore structure within stage 2 (2 min at 700 °C), where the viscous flow was at its fastest. Here, the pores were still interconnected with a glass relative density of ~75% (Fig. 2(d)). After 8 min at 700 °C (Fig. 3 (C1) and (D1)), which is at the end of stage 2 and a glass relative density of ~95%, pores were no longer interconnected and were predominantly isolated into a few large pores and a large number of small pores. This coincides with the time at which the spike in Fig. 2 (e) was observed, suggesting that pore volume was decreasing faster

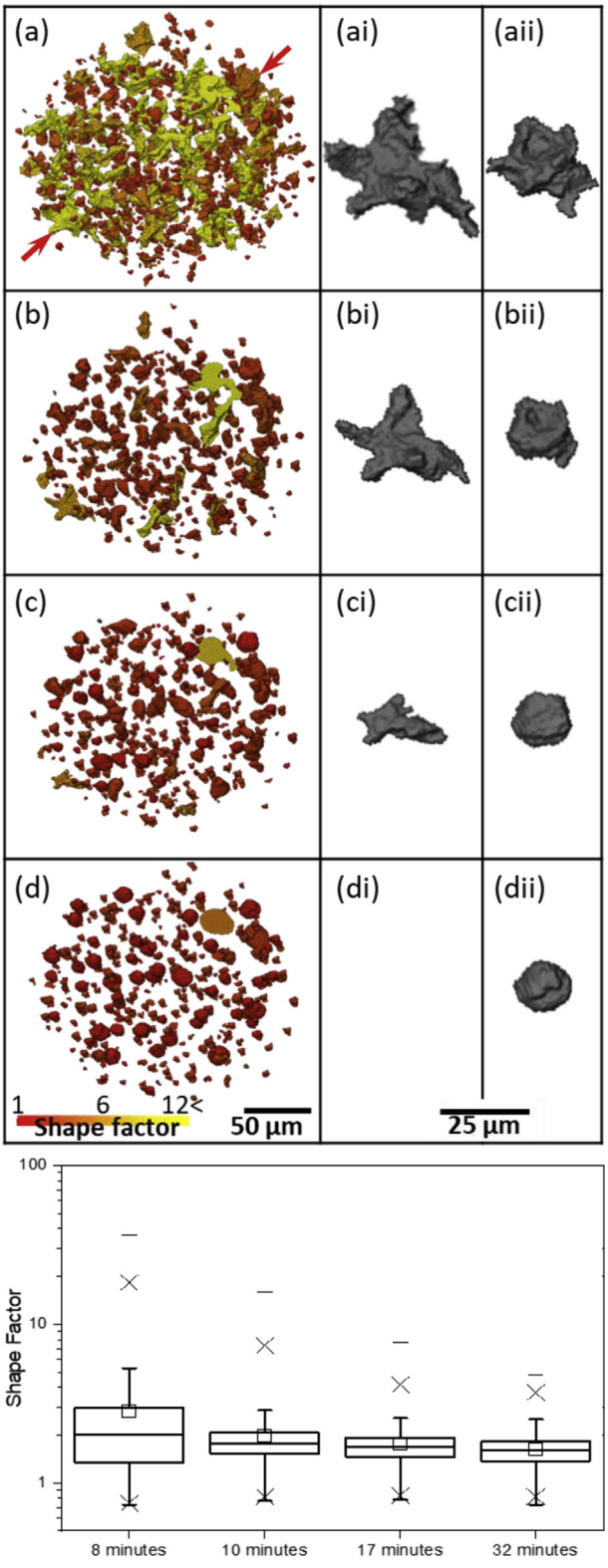

Fig. 4. Characterizing the evolution of pores from a small section of a strut of the 3D printed bioactive glass scaffold at (a) 8, (b) 10, (c) 17, and (d) 32 min into the 700 °C dwell. Column 1 shows change in shape factor, 1 being spherical and 12 being non-spherical, with time and temperature. Column 2 highlights the evolution of two pores within the volume. Column i is non-spherical and is removed, and column (ii) is spherical and does not sinter. Their locations within the volume are highlighted by the red arrows in (a). The box and whisker plot (e) quantify the global evolution of pore sphericity under the same time and temperature parameters. Where – are the maximum and minimum values, x marks the 99% and 1% and square represents the mean.

than surface area up to this point. Importantly, this observation informs that the rate of viscous flow sintering is fastest while the pores are interconnected, and once the pores became isolated, the sintering rate significantly reduces. Furthermore, this suggests that during stage 2, where >80% of overall densification takes place, pore removal is directed through the interconnected interparticle pore channels.

Fig. 3 (C3) and (D3) show the isolated pore structure after 18 min at 700 °C, where the small pores had mostly disappeared with only the large pores remaining. This corresponds to a decrease in the interparticle porosity, SA/V, in Fig. 2 (e). This is expected because the smaller pores have a larger surface area per volume, and at this temperature, it was the small pores that were observed to disappear, reducing the total pore surface area significantly. After this time, very minor changes are seen to occur, with the pores remaining similar in size but becoming more spherical. Once the pores became isolated, i.e., when the interconnectivity of the pores was lost at the end of Stage 2, further densification would be via the solvation of the gas in the pore into the glass network or via an interplay of pore pressure, viscous forces, sintering forces, and gravitational forces. If the internal pressure of the pore is equal to that of the sintering forces, there is no driving force present to remove them. Therefore, the pores remain within the scaffold structure.

Once pores became isolated, it was possible to track their progression with time within the scaffold. Pores in this study are defined as the interparticle spaces (body of air) located within the struts themselves. Their volume decreased with sintering, and eventually some of the space becomes closed pores (trapped air) once interconnectivity of the body of air was lost. The local behavior of the pore space is also related to the local silicate network connectivity, which is not taken into account here, but could be in the future, perhaps in conjunction with pore diffusion simulations which take account of local glass network connectivity. Fig. 4 and S5 offer a few initial ideas into pore morphology and its dynamical changes with sintering once the pores become closed.

One way in which shapes, or in this case pores, can be characterized is by their sphericity or shape factor (mathematical correlation), which is explained in the supplementary information S1. The concept of sphericity was introduced by Hakon Wadell [67] in 1935 and has been used to track pore evolution radiographically and topographically [54]. This concept, widely used in geology, measures the degree of 'roundness' of an object. By definition, an object has sphericity near to 1 if it approaches a perfect spherical shape ($\Psi = 1$). This value allows us to quantify the 'spherical nature' of a group of pores within the scaffolds.

Fig. 4 shows the evolution of pores from sintering for 8 to 32 min at 700 °C for a small section of a strut. Fig. 4 (a–d) show the pores color coded from red to yellow with increasing shape factor, where a shape factor (SF) of 1 (red) represents a perfect sphere and 12 (yellow) or greater represents an irregular morphology. This concept was used in this study to analyze and quantify pore evolution during sintering. With increasing time of the dwell at 700 °C, once the pores have become closed, the pores become more rounded moving to the red end of the scale, reducing their surface area, tending to an SF value of 1 (Fig. 4 (a–d)). This change is plotted in Fig. 4 (e) where the mean SF and its spread are seen to decrease with time while approaching 1.

Pores can form in scaffolds produced via direct ink writing for two reasons: air bubbles trapped in the ink during printing, which are transferred to the green body, or pores can be left because of the irregular nature of the glass particle packing in the green body. Once pores have become isolated at the end of stage 2, the only route of removal is for the gas inside to diffuse through the glass network itself. In ceramic or metal sintering, this diffusion process occurs through vacancies within the crystal structure [48]. Within a glass network, these vacancies in the classical sense do not exist. Gas solubility within glass networks has been studied and shown to give insight into the fundamentals of the glass structure such as the distribution of interstitial sites in the silicate network [68,69]. Work on the Na_2O–SiO_2 system showed that helium atoms can 'compete' with modifier ions such as sodium within the network, and it was hypothesized that oxygen can disassociate and travel through the oxygen subnetwork in the glass. To the authors' knowledge, gas permeability of air or any other gasses in bioactive glass structures has not been studied. We therefore hypothesize that owing to the more deconstructed nature of the bioactive glass networks, gas solubility would be higher than that of the more traditional glass systems.

Columns (i) and (ii) of Fig. 4 (a–d) focus on two pores from the small section of the strut, both at approximately equal distances from the edge of the strut wall (as indicated by the red arrows) and with similar volumes (Supplementary Information S5) after 8 min at 700 °C. Pore (i) was highly irregular in shape, with SF > 6, while pore (ii) was more rounded, with SF = ~3. With increasing sintering time, pore (i) reduced in size, and after 32 min at 700 °C, it completely disappeared. However, the size of pore (ii) hardly reduced and it remained within the glass throughout the sintering period.

This work gives the first 3D evidence that the sphericity of the pore dictates its ability to be removed during sintering. It is known from the study by Wakai [26] that the shrinkage and the rounding of pores are controlled by the hydrostatic and deviatoric components of the local sintering stresses, which are related to the local viscosity of glasses. As anisotropic pores shrink, our work shows that their anisotropy remains. For this to occur, diffusion of gas out of the pores must be faster than the flow of the glass into the pore

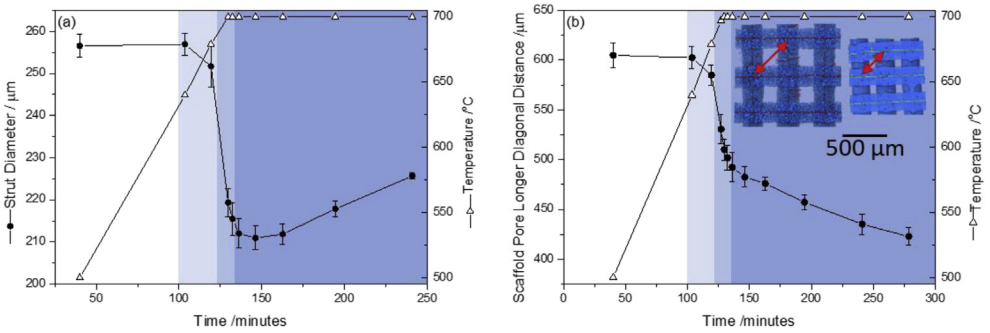

Fig. 5. (a) Strut diameter in a bioactive glass scaffold as a function of sintering time; (b) Scaffold longest diagonal distance in a bioactive glass scaffold as a function of sintering time; inset: visual representation of the longest diagonal distance on the scaffold at 500 °C and after 2.5 h at 700 °C.

as it shrinks; as, if gas diffusion was at a slower rate than the flow of the viscous glass, owing to surface tension, the pore would become spherical and not stay anisotropic [70].

High-resolution in situ X-ray tomography allows observation of the microscale sintering mechanisms, and at the same time, we gain insights into the global nature of the sintering process at the macroscale. Fig. 5 (a) measures the evolution of the scaffold strut diameter and (b) the scaffold's designed pores 'longest diagonal length' with time and temperature. The average strut diameter after binder removal was measured to be 256 ± 3 μm, which corresponds very well with the diameter of the nozzle used for printing, which was nominally ~250 μm. Once sintering began, a reduction in the strut diameter through sintering stages 1 and 2 was observed, where the particles coalesced together and densified as previously discussed. A similar trend was observed for the 'longest diagonal length' between struts for stages 1 and 2 (Fig. 5 (b)). On entering stage 3 of sintering, the strut diameter had an average size of 210 ± 3 μm, which then increased at a steady state with prolonged time at 700 °C. Within stage 3, the scaffold's 'longest diagonal length' decreased at a steady rate. The scaffold designed in this study had a woodpile structure, so the intersections of the struts created points of relatively high angle boundaries, similar to that of a particle-particle neck. Therefore, coarsening of individual struts (Fig. 5 (a) stage 3), at the global scale, to reduce surface area, will drive an isotropic reduction of the scaffold size (Fig. 5 (b) stage 3) [65]. It is interesting to note that the coarsening at the global scale is dominant only at stage 3, while coarsening at the local scale was dominant at stages 1 and 2. This suggests that there is a hierarchical order in driving force for reduction in surface area starting at the intrastrut, small particles (stage 1) followed by large particles (stage 2), and then there is a switch to global interstrut densification.

Scaffolds for bone repair are designed so that open interconnected porous channels exist to facilitate growth and repair of tissue *in vivo*. As shown by the small error bars in Fig. 5, the shrinkage of the designed pore geometries in 3D across the scaffold was uniform. This study allows the shrinkage of predesigned pores in bioactive glass scaffolds to be precisely calculated as a function of sintering temperature and time to obtain the desired porous 3D structure and consequent mechanical properties. Therefore, the ultimate goal of being able to make on-demand patient-specific scaffolds with designable geometries and pore spacings is achievable.

4. Conclusions

In situ viscous flow sintering of a bioactive glass scaffold of the 13−93 composition in 4D was studied using high-resolution synchrotron X-ray microtomography. The rates of sintering measured as surface area vs. time and temperature matched very well to the three sintering stages. The morphological evolution both at the local and global scales with time and temperature provided novel insights into the mechanism of particles coalescence and pore evolution within the glass during sintering and the designed porosity within the 3D scaffold. Results show that during Stage 1, particles lose their faceted morphology, becoming more rounded in nature with ligands and necks forming between adjacent particles while smaller particles flow and merge into larger particles. Within Stage 2, the bulk of densification takes place within a window of 16 min once the critical viscosity was reached. Here, the discrete particles coalesce to form dense struts while the interparticle porosity is removed through the connected spaces between the particles. The end of Stage 2 is marked by the remaining pores within the glass strut becoming isolated. In Stage 3, at the local scale, removal of the remaining isolated pores within the struts takes place. This was dependent on their shape, with anisotropic pores being removed and rounded pores becoming more spherical and stable. Furthermore, during Stage 3, a switch from local to global densification takes place, where the interstrut porosity begins to reduce.

This study has shown the power of synchrotron X-ray tomography further the understanding of viscous flow in a complex non-idealized model, where particles are non-spherical and both predesigned (global) and non-designed (local) porosity exist within the scaffold itself. This study provides morphological evidence for several of the predicted models of viscous flow sintering and new insights into the mechanism of densification at the local and global scales. This is the first time that these two scales of local and global densification in a porous sintered glass have been reported.

Conflict of interests

The authors declare that they have no known competing financial interests or personal relationships that could have appeared to influence the work reported in this article.

Acknowledgments

The 3D printer used in this work was funded via an EPSRC Grant for Graphene 3D networks (EP/K01658X/1). Funding for A.N-.N. was provided by RCaH-EP/I02249X/1, and the furnace was developed under the grant NE/M013561/. C.L. was sponsored by the EPSRC and MRC through Manchester's Centre for Doctoral Training (CDT) in Regenerative Medicine (EP/L014904/1). G.P. would like to acknowledge EPSRC grant EP/M023877/1. The experiment was performed on the Branchline I13-2 of the Diamond Light Source synchrotron in Oxfordshire, UK, and partly funded by the MT13241: Collaboration Proposal 1809. The authors would like to acknowledge the coworkers, Dr. Sheng Yue, Dr. Hua Geng, Dr. Jose Godinho, Dr. Kazimir Wanelik, and Dr Xiaomeng Shi for their contributions to making the beam time possible. Raw data requests are encouraged. For analysis and modeling applications, please contact Gowsihan Poologasundarampillai <g.poologasundarampillai@bham.ac.uk>.

Appendix A. Supplementary data

Supplementary data to this article can be found online at https://doi.org/10.1016/j.mtadv.2019.100011.

References

[1] L.L. Hench, H.A. Paschall, Direct chemical bond of bioactive glass-ceramic materials to bone and muscle, J. Biomed. Mater. Res. 7 (3) (1973) 25−42.
[2] I.D. Xynos, et al., Ionic products of bioactive glass dissolution increase proliferation of human osteoblasts and induce insulin-like growth factor II mRNA expression and protein synthesis, Biochem. Biophys. Res. Commun. 276 (2) (2000) 461−465.
[3] J.R. Jones, et al., Bioglass and bioactive glasses and their impact on healthcare, Int. J. Appl. Glass Sci. 7 (4) (2016) 423−434.
[4] J.R. Jones, Review of bioactive glass: From Hench to hybrids, Acta Biomaterialia, Acta Biomater 9 (1) (2013 Jan) 4457−4486.
[5] A. Nommeots-Nomm, et al., Highly degradable porous melt-derived bioactive glass foam scaffolds for bone regeneration, Acta Biomater. 57 (2017) 449−461.
[6] Q. Fu, et al., Bioactive glass scaffolds for bone tissue engineering: state of the art and future perspectives, Mater. Sci. Eng. C Mater. Biol. Appl. 31 (7) (2011) 1245−1256.
[7] L.C.R. De Jonghe, N. M, Sintering of ceramics, in: S. Somiya, F.C. Aldinger, N. Spriggs, R.M. Uchino, K. Koumoto, K. Kaneno, M. Kaneno (Eds.), Handbook of Advanced Ceramics, Academic Press, 2003, pp. 187−264.
[8] J. Massera, et al., Crystallization mechanism of the bioactive glasses, 45S5 and S53P4, J. Am. Ceram. Soc. 95 (2) (2012) 607−613.
[9] M. Cerruti, D. Greenspan, K. Powers, Effect of pH and ionic strength on the reactivity of Bioglass® 45S5, Biomaterials 26 (14) (2005) 1665−1674.
[10] O. Peitl Filho, G.P. LaTorre, L.L. Hench, Effect of crystallization on apatite-layer formation of bioactive glass 45S5, J. Biomed. Mater. Res. 30 (4) (1996) 509−514.

[11] H. Arstila, et al., Factors affecting crystallization of bioactive glasses, J. Eur. Ceram. Soc. 27 (2) (2007) 1543–1546.
[12] I. Elgayar, et al., Structural analysis of bioactive glasses, J. Non-Cryst. Solids 351 (2) (2005) 173–183.
[13] A. Hoppe, N.S. Guldal, A.R. Boccaccini, A review of the biological response to ionic dissolution products from bioactive glasses and glass-ceramics, Biomaterials 32 (11) (2011) 2757–2774.
[14] M.S. Gaafar, et al., Structural studies and mechanical properties of some borate glasses doped with different alkali and cobalt oxides, Curr. Appl. Phys. 13 (1) (2013) 152–158.
[15] A.M. Deliormanlı, In vitro assessment of degradation and bioactivity of robocast bioactive glass scaffolds in simulated body fluid, Ceram. Int. 38 (8) (2012) 6435–6444.
[16] A.M. Deliormanli, X. Liu, M.N. Rahaman, Evaluation of borate bioactive glass scaffolds with different pore sizes in a rat subcutaneous implantation model, J. Biomater. Appl. 28 (5) (2014) 643–653.
[17] Q. Fu, E. Saiz, A.P. Tomsia, Direct ink writing of highly porous and strong glass scaffolds for load-bearing bone defects repair and regeneration, Acta Biomater. 7 (10) (2011) 3547–3554.
[18] I. Ahmed, et al., Phosphate glasses for tissue engineering: Part 1. Processing and characterisation of a ternary-based P2O5-CaO-Na2O glass system, Biomaterials 25 (3) (2004) 491–499.
[19] J.C. Knowles, Phosphate based glasses for biomedical applications, J. Mater. Chem. 13 (10) (2003) 2395–2401.
[20] M. Brink, et al., Compositional dependence of bioactivity of glasses in the system Na2O-K2O-MgO-CaO-B2O3-P2O5-SiO2, J. Biomed. Mater. Res. 37 (1) (1997) 114–121.
[21] S. Fagerlund, et al., T-T-T behaviour of bioactive glasses 1–98 and 13–93, J. Eur. Ceram. Soc. 32 (11) (2012) 2731–2738.
[22] Q. Fu, et al., Mechanical and in vitro performance of 13-93 bioactive glass scaffolds prepared by a polymer foam replication technique, Acta Biomater. 4 (6) (2008) 1854–1864.
[23] K.C. Kolan, et al., Fabrication of 13-93 bioactive glass scaffolds for bone tissue engineering using indirect selective laser sintering, Biofabrication 3 (2) (2011) 025004.
[24] A. Nommeots-Nomm, P.D. Lee, J.R. Jones, Direct ink writing of highly bioactive glasses, J. Eur. Ceram. Soc. 38 (3) (2018) 837–844.
[25] X. Liu, M.N. Rahaman, Q. Fu, Oriented bioactive glass (13-93) scaffolds with controllable pore size by unidirectional freezing of camphene-based suspensions: microstructure and mechanical response, Acta Biomater. 7 (1) (2011) 406–416.
[26] F. Wakai, Mechanics of viscous sintering on the micro- and macro-scale, Acta Mater. 61 (1) (2013) 239–247.
[27] F. Wakai, et al., Sintering force behind the viscous sintering of two particles, Acta Mater. 109 (2016) 292–299.
[28] K. Katsura, et al., Sintering force behind shape evolution by viscous flow, J. Eur. Ceram. Soc. 35 (3) (2015) 1119–1122.
[29] W.D.B.,M. Kingery, Study of the initial stages of sintering solids by viscous flow, evaporation-condensation, and self-diffusion, J. Appl. Phys. 26 (10) (1955) 1205–1212.
[30] F. Varnik, et al., Simulation of viscous sintering using the lattice Boltzmann method, Model. Simul. Mater. Sci. Eng. 21 (2) (2013) 025003.
[31] R.M.C.V. Reis, et al., Sintering and rounding kinetics of irregular glass particles, J. Am. Ceram. Soc. 102 (2) (2019) 845–854.
[32] M.N. Rahaman, et al., Creep and densification during sintering of glass powder compacts, J. Am. Ceram. Soc. 70 (10) (1987) 766–774.
[33] I.B. Cutler, R.E. Henrichsen, Effect of particle shape on the kinetics of sintering of glass, J. Am. Ceram. Soc. 51 (10) (1968), 604-604.
[34] M.T. Souza, et al., Effect of magnesium ion incorporation on the thermal stability, dissolution behavior and bioactivity in Bioglass-derived glasses, J. Non-Cryst. Solids 382 (2013) 57–65.
[35] H.L. Friedman, Kinetics of thermal degradation of char-forming plastics from thermogravimetry. Application to a phenolic plastic, J. Polym. Sci. Part C: Polymer Symposia 6 (1) (1964) 183–195.
[36] J. Massera, et al., Crystallization behavior of phosphate glasses and its impact on the glasses' bioactivity, J. Mater. Sci. 50 (8) (2015) 3091–3102.
[37] S. Kashyap, K. Griep, J.A. Nychka, Crystallization kinetics, mineralization and crack propagation in partially crystallized bioactive glass 45S5, Mater. Sci. Eng. C 31 (4) (2011) 762–769.
[38] D.U. Tulyaganov, et al., Synthesis, processing and characterization of a bioactive glass composition for bone regeneration, Ceram. Int. 39 (3) (2013) 2519–2526.
[39] M.O. Prado, E.D. Zanotto, Glass sintering with concurrent crystallization, Compt. Rendus Chem. 5 (11) (2002) 773–786.
[40] W. Panna, P. Wyszomirski, P. Kohut, Application of hot-stage microscopy to evaluating sample morphology changes on heating, J. Therm. Anal. Calorim. 125 (3) (2016) 1053–1059.
[41] P.A. Tick, et al., Hot stage optical microscopy studies of crystallization in fluoride glass melts, J. Non-Cryst. Solids 140 (1992) 275–280.
[42] L. Lefebvre, et al., Sintering behaviour of 45S5 bioactive glass, Acta Biomater. 4 (6) (2008) 1894–1903.
[43] D. Bernard, et al., First direct 3D visualisation of microstructural evolutions during sintering through X-ray computed microtomography, Acta Mater. 53 (1) (2005) 121–128.
[44] D. Bernard, et al., Constrained sintering of glass films: microstructure evolution assessed through synchrotron computed microtomography, Acta Mater. 59 (16) (2011) 6228–6238.
[45] M. Wallenstein, et al., Qualitative and quantitative insights into multiphase flow in ceramic sponges using X-ray computed tomography, Chem. Eng. Sci. 138 (2015) 118–127.
[46] D. Bouttes, et al., Hydrodynamic coarsening in phase-separated silicate melts, Acta Mater. 92 (2015) 233–242.
[47] J. Villanova, et al., Fast in situ 3D nanoimaging: a new tool for dynamic characterization in materials science, Mater. Today 20 (7) (2017) 354–359.
[48] D. Uskoković, H.E. Exner, The kinetics of contact formation during sintering by diffusion mechanisms, in: S. Sōmiya, Y. Moriyoshi (Eds.), Sintering Key Papers, Springer Netherlands, Dordrecht, 1990, pp. 111–146.
[49] C. Rau, et al., Coherent imaging at the Diamond beamline I13, Phys. Status Solidi 208 (11) (2011) 2522–2525.
[50] Z.D. Pešić, et al., Experimental stations at I13 beamline at Diamond light Source, J. Phys. Conf. Ser. 425 (18) (2013) 182003.
[51] C. Puncreobutr, et al., Quantitative 3D characterization of solidification structure and defect evolution in Al alloys, J. Occup. Med. 64 (1) (2012) 89–95.
[52] K.M. Kareh, et al., Revealing the micromechanisms behind semi-solid metal deformation with time-resolved X-ray tomography, Nat. Commun. 5 (2014) 4464.
[53] S. Karagadde, et al., Transgranular liquation cracking of grains in the semi-solid state, Nat. Commun. 6 (2015) 8300.
[54] B. Cai, et al., Time-resolved synchrotron tomographic quantification of deformation during indentation of an equiaxed semi-solid granular alloy, Acta Mater. 105 (2016) 338–346.
[55] A.C. Kak, M. Slaney, Principles of Computerized Tomographic Imaging, IEEE Press, 1988.
[56] R.C. Atwood, et al., A high-throughput system for high-quality tomographic reconstruction of large datasets at Diamond Light Source, Phil. Trans. Math. Phys. Eng. Sci. 373 (2043) (2015) 20140398.
[57] M.C. Strotton, et al., Optimising complementary soft tissue synchrotron X-ray microtomography for reversibly-stained central nervous system samples, Sci. Rep. 8 (1) (2018) 12017.
[58] M. Basham, et al., Data analysis WorkbeNch (DAWN), J. Synchrotron Radiat. 22 (3) (2015) 853–858.
[59] P.D. Lee, J.D. Hunt, Hydrogen porosity in directional solidified aluminium-copper alloys:in situ observation, Acta Mater. 45 (10) (1997) 4155–4169.
[60] A. Chaijaruwanich, et al., Pore evolution in a direct chill cast Al–6wt.% Mg alloy during hot rolling, Acta Mater. 54 (19) (2006) 5185–5194.
[61] J.R. Jones, et al., Non-destructive quantitative 3D analysis for the optimisation of tissue scaffolds, Biomaterials 28 (7) (2007) 1404–1413.
[62] J.C. Mauro, et al., Viscosity of glass-forming liquids, Proc. Natl. Acad. Sci. U. S. A. 106 (47) (2009) 19780–19784.
[63] Q. Fu, J.C. Mauro, M.N. Rahaman, Bioactive glass innovations through academia-industry collaboration, Int. J. Appl. Glass Sci. 7 (2) (2016) 139–146.
[64] R. Meszaros, et al., Three-Dimensional Printing of a Bioactive Glass, vol. 52, 2011, pp. 111–116.
[65] S.-J.L. Kang, 4 – Initial Stage Sintering, in: S.-J.L. Kang (Ed.), Sintering, Butterworth-Heinemann, Oxford, 2005, pp. 39–55.
[66] E. Liniger, R. Raj, Packing and sintering of two-dimensional structures made from bimodal particle size distributions, J. Am. Ceram. Soc. 70 (11) (1987) 843–849.
[67] H. Wadell, Volume, shape, and roundness of quartz particles, J. Geol. 43 (3) (1935) 250–280.
[68] N.P. Bansal, R.H. Doremus, Chapter 17 – solubility, permeability, and diffusion of gases in glass, in: N.P. Bansal, R.H. Doremus (Eds.), Handbook of Glass Properties, Academic Press, San Diego, 1986, pp. 607–645.
[69] J.F. Shackelford, Gas solubility and diffusion in oxide glasses – implications for nuclear wasteforms, Procedia Mater. Sci. 7 (2014) 278–285.
[70] K.L. Walker, et al., Consolidation of participate layers in the fabrication of optical fiber preforms, J. Am. Ceram. Soc. 63 (1-2) (1980) 96–102.